

Development of Zr- and Gd-doped porous ceria (pCeO_2) abrasives for achieving high-quality and high-efficiency oxide chemical mechanical polishing

Ailian Chen^a, Shirui Wang^a, Jie Pan^b, Tianyu Wang^a, Yang Chen^{b,*}

^a School of Mechanical Engineering, Changzhou University, Changzhou, Jiangsu, 213164, PR China

^b School of Materials Science and Engineering, Changzhou University, Changzhou, Jiangsu, 213164, PR China



ARTICLE INFO

Keywords:

Porous CeO_2
Doping
Oxygen vacancy
Nanostructure
Abrasive
Chemical mechanical polishing

ABSTRACT

Porous ceria (pCeO_2), Zr-doped pCeO_2 (pCeZrO_2), and Gd-doped pCeO_2 (pCeGdO_2) abrasives for both surface quality and removal rate improvements were developed using a facile one-pot solvothermal approach. The resulting products were characterized via XRD, SEM, TEM, HRTEM, Raman spectroscopy, UV-visible spectroscopy, and N_2 adsorption-desorption measurements. Raman spectra revealed that oxygen vacancies were the dominant defects in pCeO_2 nanospheres. Zr- and Gd-doping treatments contributed to oxygen vacancy enrichment, thus leading to an increased content of trivalent cerium (Ce^{3+}) formed on the pCeO_2 surfaces. Oxide-CMP capability of pure pCeO_2 , pCeZrO_2 , and pCeGdO_2 abrasives were compared in terms of surface morphology/roughness/defect, topographical variation, as well as material removal rate (*MRR*). Atomic force microscopy and interferometric microscopy investigations showed that both pCeO_2 , pCeZrO_2 , and pCeGdO_2 abrasives achieved high-quality surfaces with ultra-low roughness (0.11–0.14 nm Ra, 0.13–0.17 nm RMS). As expected, the *MRR* was accelerated by 78.7% in alkaline slurries containing pCeGdO_2 abrasives compared to the undoped pCeO_2 . The improved CMP performance might be attributed to the reduced modulus, the expand pore size, as well as the enriched Ce^{3+} and oxygen vacancy. Furthermore, the interfacial action and removal mechanism of the pCeO_2 abrasives were discussed on the basis of their structure feature and surface chemistry.

1. Introduction

Chemical mechanical polishing (CMP) [1–5] is one of the most effective and available techniques for surface global planarization, which has been widely applied in the manufacturing of integrated circuits (IC), micro-electromechanical system, hard disk, ceramic, metal, etc. It is generally believed that a typical CMP process involves and combines chemical surface corrosion and mechanical (or tribomechanical) material removal. The purpose of CMP is to eliminate the mechanical damages originated from earlier grinding and/or polishing processes and to create ultra-smooth surfaces. CMP performance is mainly affected by the morphological, structural, and physicochemical properties of abrasives.

In a typical CMP process, particle abrasives in polishing slurries are the primary participants in mechanical energy transmission and chemical surface modification. Typically, 100–300 nm abrasive NPs are available in various CMP applications. The useful properties and

successful applications of abrasive systems are a consequence of the physical and structural characteristics of these nanoparticles (NPs), and their mechanical property and surface chemistry. Theoretical analyses and experimental investigations reveal that porous abrasives [6–15] contribute to the improvements of both surface quality and/or removal efficiency in polishing and grinding processes. It may be attributed to their relative-high elastic responses (or relative-low elastic moduli) under an applied down force, and thus resulting in a reduced contact stress and an enlarged contact area between the abrasive and the surface. The optimized interfacial contact behavior may be responsible for the improved polishing or grinding performances. Up to now, available investigations on porous abrasives mainly focus on (polymer-modified or copper-incorporated) Al_2O_3 [6–8], $\text{Fe}_2\text{O}_3/\text{SiO}_2$ [9], cubic boron nitride (CBN) [10], diamond [11], and SiO_2 [12–15] materials. Among these porous abrasives, porous SiO_2 (pSiO_2) particles have the advantages of simple synthesis, good sphericity, uniform morphology, narrow particle size-distribution, controlled particle size, as well as tunable pore

* Corresponding author.

E-mail address: cy.jpu@126.com (Y. Chen).

diameter and pore structure.

In our previous work [12], the pSiO₂ (200–500 nm) spheres with radially oriented channels (2–3 nm of average pore size) were prepared via a modified Stöber approach in the presence of cetyltrimethylammonium bromide as a template agent. Oxide-CMP results showed that the pSiO₂ abrasives contributed to removal rate enhancement as well as surface roughness and topographical variation reductions, compared to the non-porous SiO₂ ones. As reported by Ryu and coworkers [13], the wrinkled pSiO₂ NPs with uniform sizes of 65–400 nm were also developed by applying a cooling stage to the reaction mixture, and proposed as novel abrasives for improved oxide-CMP performance. In our subsequent work [14], the pSiO₂ spheres (ca. 80 nm) with dendritic-like structures and controlled average pore size (3–6 nm) were fabricated via an oil-water biphasic stratification method. It was also revealed that decreased pSiO₂ particle sizes and/or expanded pore sizes contributed to surface quality and polishing efficiency increases, possibly resulting from the enlarged real contact area, promoted tribo-chemical wear, and enhanced adhesion action. These provided data were accordance with the molecular dynamics (MD) simulations as described in literature [16]. And it was further suggested that the contact-area-based mechanism and contact-penetration-adhesion model might be predominant during CMP processes. Recently, Gao and coworkers [15] reported the synthesis of rod-shaped pSiO₂ abrasives for improved surface quality of cadmium zinc telluride wafers. It is commonly recognized that the superior CMP performance may result from the low modulus and elastic deformability of pSiO₂ abrasives under an applied force. In spite of the several reports on pSiO₂ abrasive NPs, little is known about the CMP applications of porous CeO₂ (pCeO₂) abrasives.

In CMP applications, the type, size and distribution, structure, and shape of particle abrasives play a key role in determining the surface morphology, roughness, defect and damage, as well as the material removal efficiency. Among the commonly used abrasive systems, CeO₂ NPs have the advantages of high removal efficiency over silica and high selectivity of oxide and nitride [17–22]. However, the CeO₂ NPs synthesized by solvothermal, sol-gel, hydrothermal and other methods are commonly irregular in shapes with relatively broad particle-size distributions, which easily scratch surfaces and introduce damages or defects. CMP performance highly depends on the morphologic characteristics of abrasives, and various surface defects may be caused by non-spherical shapes. As a result, the CMP applications of CeO₂ NPs in IC manufacturers are highly limited by comparison with other spherical abrasives (typically colloidal SiO₂). For superior CMP property, spherical particles may be more ideal due to the substitution of sliding friction with rolling friction at the interfacial contact between abrasives and surfaces [17]. However, it is still a challenge for fabricating spherical CeO₂ NPs, and thus restricting further improvement of polishing capability and comprehensive understanding of material removal behavior.

To the best of our knowledge, there are few reports on CMP applications of pCeO₂ abrasives for improving both surface quality and removal efficiency. Herein, we report a simple one-pot approach for fabricating uniform pure, Zr- and Gd-doped pCeO₂ nanospheres with high specific area and well-defined structure, as well as their usage as novel abrasives for optimized oxide-CMP performance. The resulting samples were characterized by powder X-ray diffraction, field emission scanning electron microscopy, transmission electron microscopy (TEM), high-resolution TEM, Raman spectroscopy, diffuse reflectance UV-vis spectroscopy, and nitrogen adsorption-desorption measurements. The surface features were evaluated using an atomic force microscope and a non-contact profiler. The developed pCeO₂ and pCeZrO₂ abrasives revealed superior CMP performance toward silica films by comparison with the reported results. The possible interfacial contact and removal mechanism of the proposed pCeO₂ abrasives were also discussed according to their structure feature and surface chemistry. The aim of work is expected to provide some useful insights into the structure and property regulations of CeO₂-based abrasives.

2. Experimental section

2.1. Synthesis

Uniform pCeO₂ NPs were prepared via a solvothermal approach [23] with a little modification. In a typical synthesis, 1.5 mL of deionized water was added to 45 mL of ethylene glycol (EG, AR) solution containing 1.5 g of cerium nitrate (Ce(NO₃)₃·6H₂O, AR). And the mixture was ultrasonically treated for 5 min. Then, 1.5 mL of acetic acid (CH₃COOH, AR) was added dropwise into the solution mentioned above. After treatment by sonication, the mixed solution was sealed and heated to 180 °C for 3 h. The resulting precipitates were collected by centrifugation (10000 r/min), washed with deionized water and ethanol, dried in air at 80 °C overnight, and finally calcined at 500 °C in air for 1 h.

For comparison, Zr- and Gd-doped pCeO₂ (pCe_{1-x}Zr_xO₂ and pCe_{1-x}Gd_xO₂, x = 0.15) NPs were also fabricated according to the procedure described above with small modifications, where x was the molar ratio of Zr/(Ce + Zr) or Gd/(Ce + Gd) with a value of 0.15. Identical conditions as the previous syntheses were applied, except that 1.7 g of Ce (NO₃)₃·6H₂O and 0.16 g of zirconium oxynitrate hydrate (ZrO (NO₃)₂·xH₂O, AR) were used for the pCeZrO₂ synthesis. In the case of pCeGdO₂ NPs, 1.7 g of Ce(NO₃)₃·6H₂O and 0.31 g of gadolinium nitrate (Gd(NO₃)₃·6H₂O, AR) were used.

2.2. Characterizations

The crystal phases of the products were determined with a D/Max 2500 PC powder X-ray diffractometer (XRD, Rigaku) operating with Cu K α (λ = 1.54056 Å) radiation by 2θ ranging from 10° to 80°. Raman spectra was recorded using a DXR spectrometer (Thermo Fisher). Nitrogen adsorption-desorption measurements were performed on a TriStar 3020 analyzer (Micrometrics) at 77 K. The specific surface area was calculated using the Brunauer-Emmett-Teller (BET) model, and the pore-size distributions were calculated from the absorption branch data using the Barrett-Joyner-Halenda (BJH) method. The structure and morphology of the samples were characterized using a SUPRA 55 field emission scanning electron microscope (FESEM, ZEISS) performing at an accelerating voltage of 5 kV, and a JEM-2100 transmission electron microscope (TEM, JEOL) operating at an accelerating voltage of 120 kV. UV-vis diffuse reflectance spectra (UV-vis DRS) were recorded using a Shimadzu UV-3600 spectrophotometer.

2.3. CMP experiments

The SiO₂ layer was a 1200-nm thermal oxide film on a 4-inch silicon wafer obtained from Huacheng Changban Microelectronics Co., Ltd. (Changzhou, China), which was cut into square workpieces (ca. 20 mm in width and ca. 0.75 mm in thickness) and mounted on a metal piece for testing. The substrates were polished with the usage of a TegraForce-1/TegraPol-15 polisher (Struers, Denmark) coupled with a porous polyurethane pad (MD-Chem, Struers) at an applied down pressure of 3.0 psi. The rotation speed of the pad and the head was 90 and 120 rpm, respectively. The polishing time and slurry flow rate was 2 min and 50 mL/min, respectively. The polishing slurry mixture with a solid content of 1 wt% was adjusted to pH 8.5 with the use of 0.1 M NaOH, and was treated by sonication for 10 min prior to use. After CMP experiments, the workpieces were cleaned by sonication in acetone and deionized water, dried and stored in nitrogen prior to further surface analyses.

High-resolution morphology analyses were performed on a Nanonano VS atomic force microscope (AFM, VEECO, currently Bruker) equipped with a Dimension V controller in tapping mode under ambient conditions of 20 °C and 40% relative humidity. Standard silicon AFM probes (Tap300Al-G, BudgetSensors, with aluminum reflective coating) were used in all AFM measurements. The typical tip radius was less than 10 nm and the half cone angle was ca. 10° at the apex, as specified by the

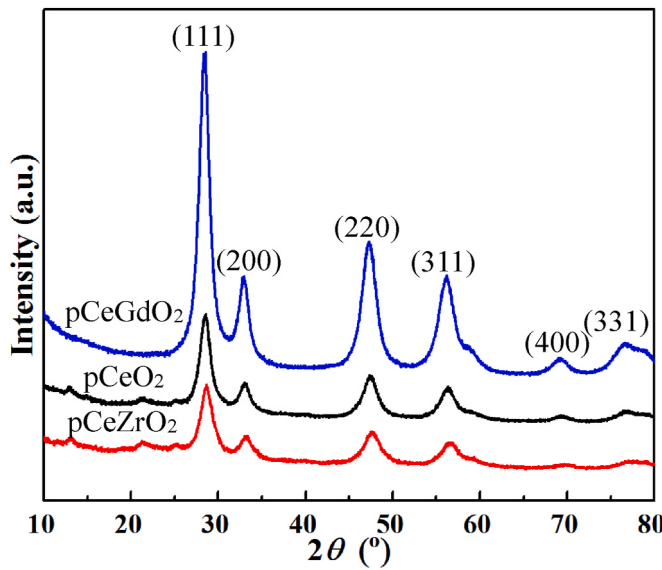


Fig. 1. XRD patterns of the as-obtained pCeO₂, pCeZrO₂, and pCeGdO₂ samples.

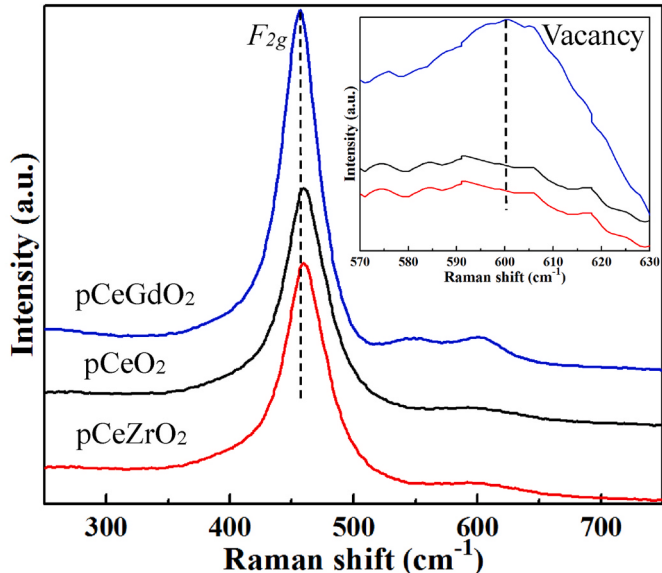


Fig. 2. Raman spectra of pCeO₂, pCeZrO₂, and pCeGdO₂ samples.

manufacturer. The scanning rate was 1Hz, and the pixels per line were 256. And the scanning scale were chosen the same for all AFM experiments ($5.0 \times 5.0 \mu\text{m}^2$). For the surfaces before and after CMP, the average roughness (R_a) and root-mean-square (RMS) data were determined within $5.0 \times 5.0 \mu\text{m}^2$. In addition, the three-dimensional (3D) AFM images and the line-scan profiles were derived from the corresponding two-dimensional (2D) AFM height images using the NanoScope Analysis Software (V 1.40, Bruker).

The surface topographies in a large scale ($180.8 \times 241.0 \mu\text{m}^2$) were also tracked by a 3D non-contact surface profiler (ContourGT-K0, Bruker). Material removal rate (MRR , nm/min) was defined as the SiO₂ thickness difference before and after CMP in unit time, and calculated using a weight-loss method [24,25]. The mass difference of the workpiece before and after CMP was measured by analytical electron balance (XS105, Mettler Toledo, Switzerland, exact to 0.01 mg). Herein, the provided roughness and MRR data were the average of three runs.

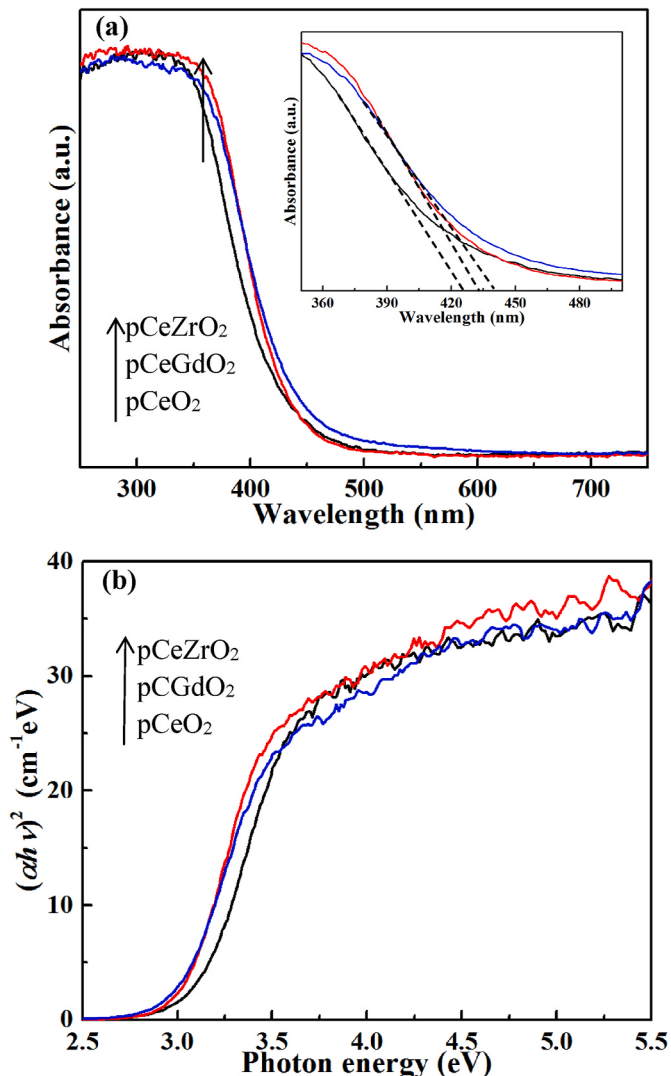


Fig. 3. UV-vis diffuse reflectance spectra (a) and the corresponding Tauc plots (b) of pCeO₂, pCeZrO₂, and pCeGdO₂ samples.

3. Results and discussion

3.1. Structure and morphology analyses

Fig. 1 shows the XRD patterns of the as-obtained pCeO₂, pCeZrO₂, and pCeGdO₂ samples. The positions of the diffraction peaks and their respective planes in the XRD patterns are well consistent with the reported data of CeO₂ materials (JCPDS 34–0394), confirming the formation of the cubic fluorite crystalline phase [26]. No additional diffraction peaks can be found in the XRD pattern of the pCeZrO₂ and pCeGdO₂ products, suggesting that the crystalline phase does not alter when the dopant is added to the host lattice. As estimated by the Scherrer's formula from (111) planes, the crystallite sizes of the pure, Zr-doped pCeO₂ and Gd-doped pCeO₂ were calculated to be 7.2 nm, 6.8 nm, and 7.1 nm, respectively. And the lattice parameters of pCeO₂, pCeZrO₂, and pCeGdO₂ NPs were determined to be 5.422 Å, 5.413 Å, and 5.419 Å, respectively. In addition, the diffraction peaks of pCeZrO₂ are slightly shifted towards higher 2θ values compared to the undoped ones [27]. The ionic radius of Zr⁴⁺ (0.084 nm) and Gd³⁺ (0.094 nm) are slightly smaller than that of Ce⁴⁺ (0.097 nm) [28,29], which is responsible for the high-angle shift and lattice compression.

Raman spectrum is an effective and non-destructive method for detecting structure and surface defects of CeO₂ materials. As illustrated

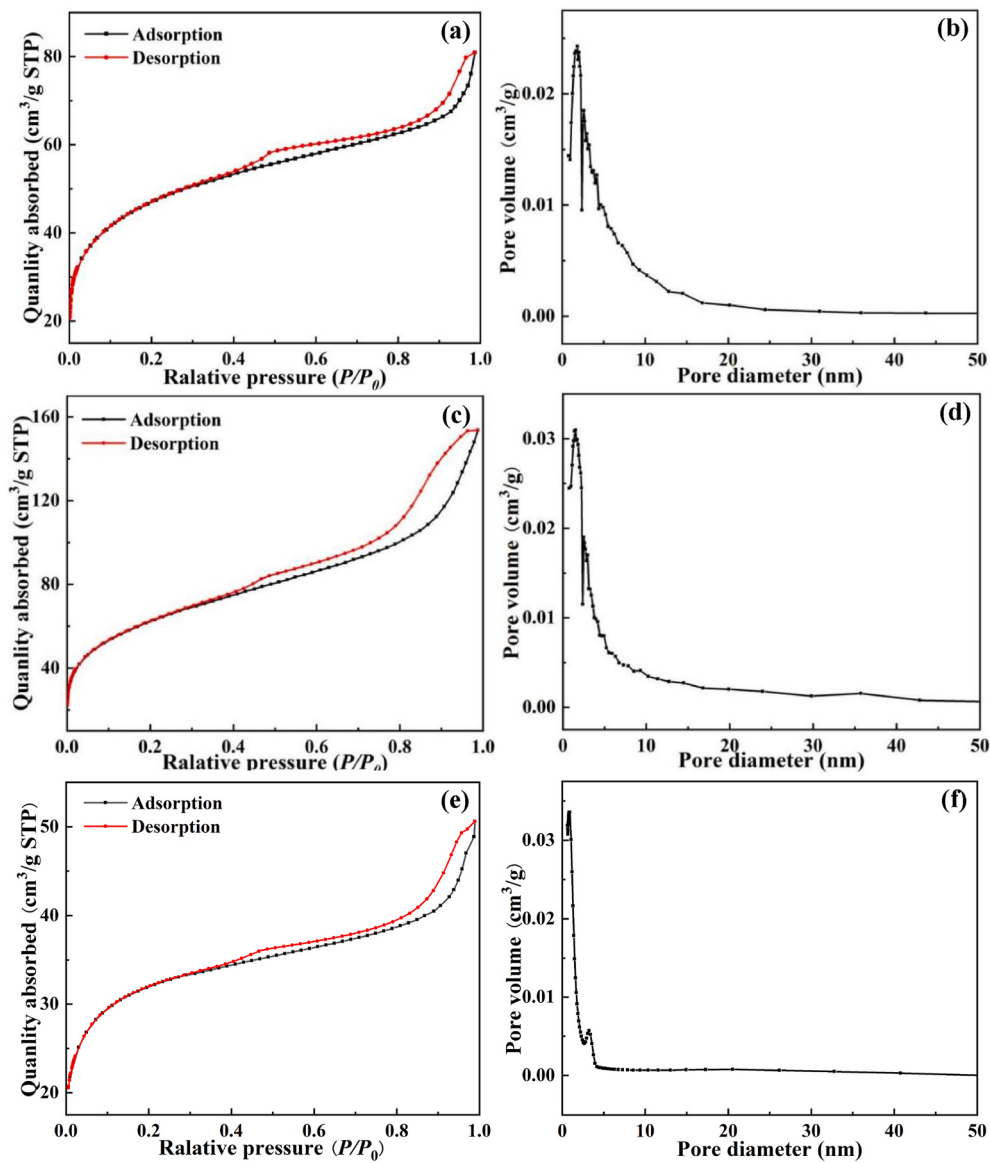


Fig. 4. Nitrogen adsorption-desorption isotherms and pore-size distributions of (a, b) pCeO₂, (c, d) pCeZrO₂, and (e, f) pCeGdO₂ samples.

In Fig. 2, the distinct peaks located at 460–465 cm⁻¹ in the Raman spectra further reveal the F_{2g} symmetric stretching of Ce–O bonds in Ce–O8 vibrational units of fluorite cubic-phase CeO₂ (space group $Fm\bar{3}m$). For the Zr- and Gd-doped pCeO₂ NPs, the presence of Ce³⁺ and oxygen defects changes Ce–O bond lengths, shifting the F_{2g} mode center towards relatively high wavenumbers by comparison with undoped ones. Another weak peak at ~600 cm⁻¹ is also assigned to the oxygen related defects in CeO₂ lattices (typically oxygen vacancies) [30]. It commonly recognized that the I_{600}/I_{460} ratio can reflect the oxygen vacancies and lattice deformations. And an increased I_{600}/I_{460} ratio indicates the enhanced content of surface defects (typically Ce³⁺ and oxygen vacancies). In this work, the pCeZrO₂ and pCeGdO₂ samples exhibit much higher intensity ratio of I_{600}/I_{460} (0.099 and 0.104) than that of the undoped pCeO₂ (ca. 0.048), suggesting the increased concentrations of oxygen vacancy and Ce³⁺ in CeO₂ [31].

The optical properties of the pCeO₂, pCeZrO₂, and pCeGdO₂ were evaluated via UV-vis diffuse absorption spectroscopy. As shown the UV-vis spectra (Fig. 3a), the pCeO₂, pCeZrO₂, and pCeGdO₂ samples present strong absorption properties in the ultraviolet range. In addition, the absorption edge of the pCeZrO₂ (433 nm) and pCeGdO₂ (441 nm) products are shifted over a higher wavelength region (red shift)

compared to the undoped pCeO₂ ones (426 nm). The red-shift absorption edge of the pCeZrO₂ and pCeGdO₂ may be attributed to the charge transfer from CeO₂ to metal atoms, and associated with lattice defects caused by Zr- and Gd-doping. UV-DRS spectra were further transformed using the Kubelka-Munk function to eliminate the band gaps. The plots of K-M function versus the energy of absorbed light are shown in Fig. 3b. The band gap values of pCeO₂, pCeZrO₂, and pCeGdO₂ were calculated to be 3.12 eV, 3.04 eV, and 3.01 eV respectively, indicating that Zr- and Gd-doping can induce the narrowed band gap of CeO₂. It is commonly believed that the doping of metal cations in CeO₂ contribute to the formation of trivalent cerium (Ce³⁺) and create more oxygen vacancies. Consequently, the red shifting in the band gap may be attributed to the formation of intermediate state or doping-related transition state [32, 33], originating from the increased concentrations of oxygen vacancy and Ce³⁺. The presented results imply that the pCeZrO₂ and pCeGdO₂ possess high Ce³⁺ and oxygen vacancy concentrations compared to the undoped pCeO₂ ones. In this work, both Raman and UV-vis results further suggest that the pCeGdO₂ products have the relatively highest contents of surface defects, such as Ce³⁺ and oxygen vacancy.

Nitrogen adsorption-desorption isotherms of the as-obtained products (Fig. 4a, c, e) exhibit representative type-IV isotherms with type-H2

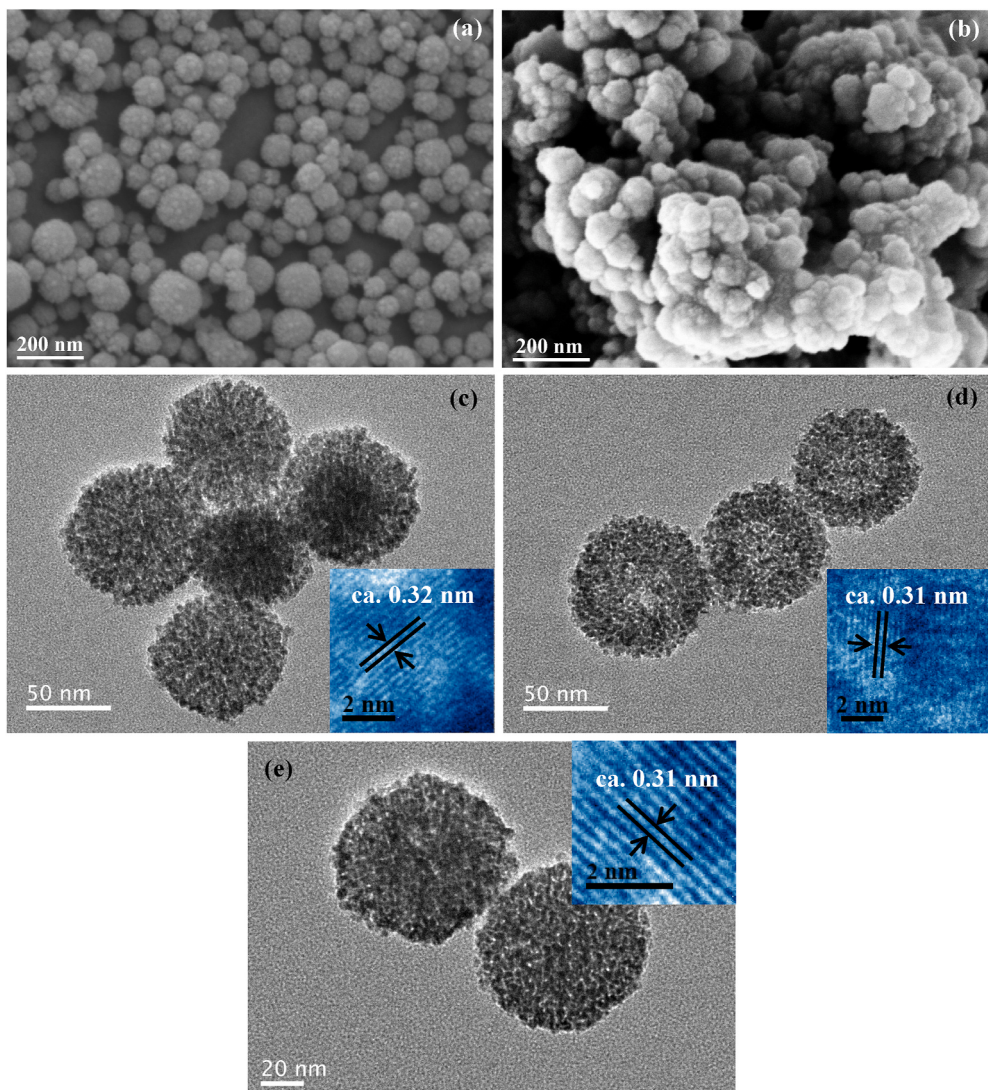


Fig. 5. FESEM, TEM, and HRTEM (inset) images of (a, c) pCeO₂, (b, d) pCeZrO₂, and (e) pCeGdO₂ samples.

hysteresis loops, indicating the porous natures of the samples (resulted from the packing of CeO₂ NPs) [34]. The BET specific area of pCeO₂, pCeZrO₂, and pCeGdO₂ samples are around 195 m²/g, 176 m²/g, and 110 m²/g, respectively. As shown in Fig. 4b, d, and f, the pore-size distributions are narrowly distributed and mainly centered below 10 nm. As calculated from the adsorption branch data, the average pore size of pCeO₂, pCeZrO₂, and pCeGdO₂ samples were determined to be 5.1 nm, 6.9 nm, and 8.1 nm, respectively.

As shown in Fig. 5a and b, FESEM observations clearly reveal that most pCeO₂ and pCeZrO₂ samples have uniform and spherical shapes. The pCeZrO₂ and pCeGdO₂ samples present a relatively small particle size (60–80 nm) compared to that of the pCeO₂ ones (70–90 nm). In addition, TEM observations (Fig. 5c, d, and e) provide more information about the microstructures of the pCeO₂, pCeZrO₂, and pCeGdO₂ products. It demonstrates that the nanospheres are consisted of minor CeO₂ NPs (~5 nm), and many irregular mesopores coexist. Distinct lattice fringes can also be clearly observed from the high-resolution TEM (HRTEM) images (inset). And the interplanar distances of pCeO₂, pCeZrO₂, and pCeGdO₂ are 0.32 nm, 0.31 nm, and 0.31 nm respectively, which can be assigned to the (111) planes of CeO₂. The slightly reduced lattice spacings also prove the successful Zr- or Gd-doping into CeO₂ nanocrystals.

3.2. CMP performances

3.2.1. Surface analysis and removal rate

Surface quality and removal efficiency are crucial evaluating indicators towards successful CMP applications. The type, structure, and property of particle abrasives play a key role in determining the achieved performance. Herein, the SiO₂-CMP tests focused on the dependency of physicochemical properties of pCeO₂ and pCeZrO₂ abrasives on the final CMP characteristics. In this work, 2D- and 3D-topography, surface roughness, as well as the line-scan profile of the workpieces before and after CMP were explored using a high-resolution AFM. For sectional profile analyses, the two diagonals in 2D-AFM height images are selected for the line-scan measurements and further comparisons. As presented in Fig. 6a, the color difference or distribution inhomogeneity can be clearly observed from the 2D-AFM height image, implying the rough appearance of the original surface. And the *Ra* and *RMS* roughness within $1.0 \times 1.0 \mu\text{m}^2$ were measured to be 0.99 nm and 1.25 nm, respectively. The corresponding line-scan trace (Fig. 6b) along the dotted line in the AFM-height image reveals the maximum peak height (MPH) of 2.9 nm and the maximum valley depth (MVD) of 3.2 nm.

AFM results clearly reveal that the proposed pCeO₂, pCeZrO₂, and pCeGdO₂ abrasives achieve ultra-smooth and damage-free surfaces. As shown in Figs. 7a, 8a and 9a, the improved uniformity in AFM-height

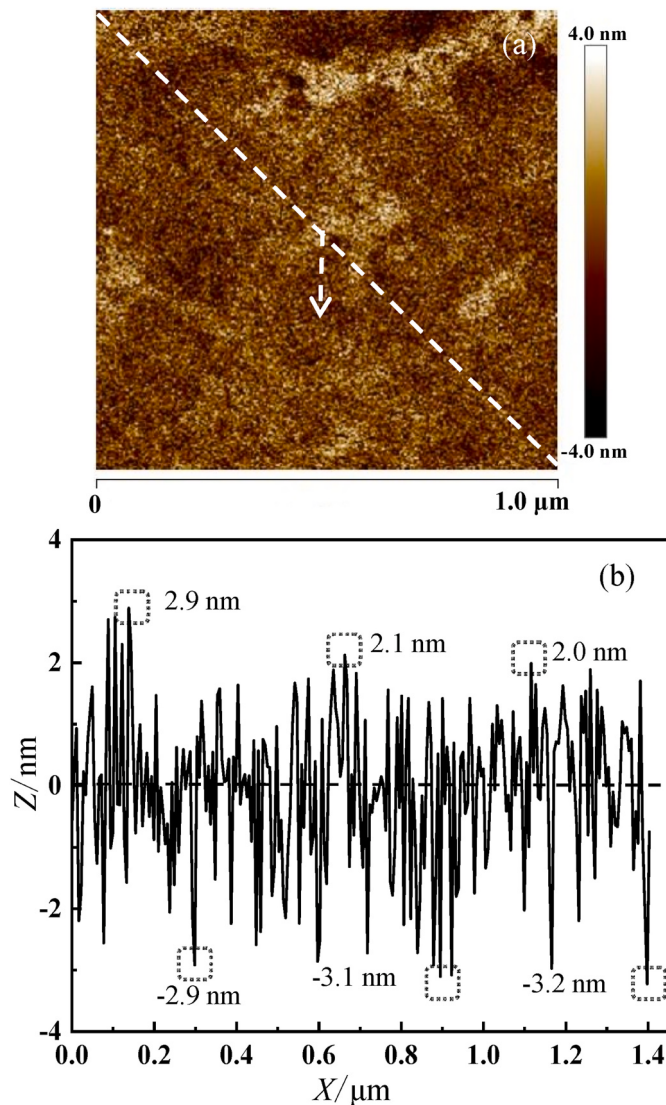


Fig. 6. 2D-AFM image (a) and the corresponding line-scan profile (b) of the surface prior to CMP.

images suggest superior surface quality and flatness. The R_a and RMS roughness within $5.0 \times 5.0 \mu\text{m}^2$ achieved by pCeO₂ abrasives are $0.11 \pm 0.02 \text{ nm}$ and $0.14 \pm 0.03 \text{ nm}$, which are comparable to those of pCeZrO₂ ($0.11 \pm 0.01 \text{ nm } R_a$, $0.13 \pm 0.01 \text{ nm RMS}$) and pCeGdO₂ ($0.14 \pm 0.03 \text{ nm } R_a$, $0.17 \pm 0.03 \text{ nm RMS}$) abrasives. It may be attributed to their similar mechanical properties, such as elastic modulus, surface hardness, etc. The pure, Zr- and Gd-doped pCeO₂ abrasives allow the surfaces to be brought to atomic-scale roughness, illustrating their application potentials in ultra-precise processing. As shown in Fig. 7b, the resulting line-traces (Lines 1 and 2) indicate that the pCeO₂ abrasives achieve a topographical variation of $\pm 0.25 \text{ nm}$ (0.25 nm of the MPH and 0.18 nm of the MVD). In the case of pCeZrO₂ (Fig. 8b), the corresponding line-traces (Lines 3 and 4) also reveal a comparable topographical variation of $\pm 0.28 \text{ nm}$ (0.25 nm of the MPH and 0.28 nm of the MVD). For the pCeGdO₂ abrasives (Fig. 9b), the line-traces (Lines 5 and 6) demonstrate the MPH of 0.32 nm and the MVD of 0.25 nm . A comparison with the initial surface ($\pm 3.2 \text{ nm}$, Fig. 6b) clearly confirm that both pCeO₂, pCeZrO₂, and pCeGdO₂ abrasives contribute to the obviously improved planarization degrees. The roughness data of the surfaces before and after CMP are summarized in Table 1.

Morphology changes of the surfaces before and after polishing can be distinctly observed from the 3D-AFM images. Compared to the initial

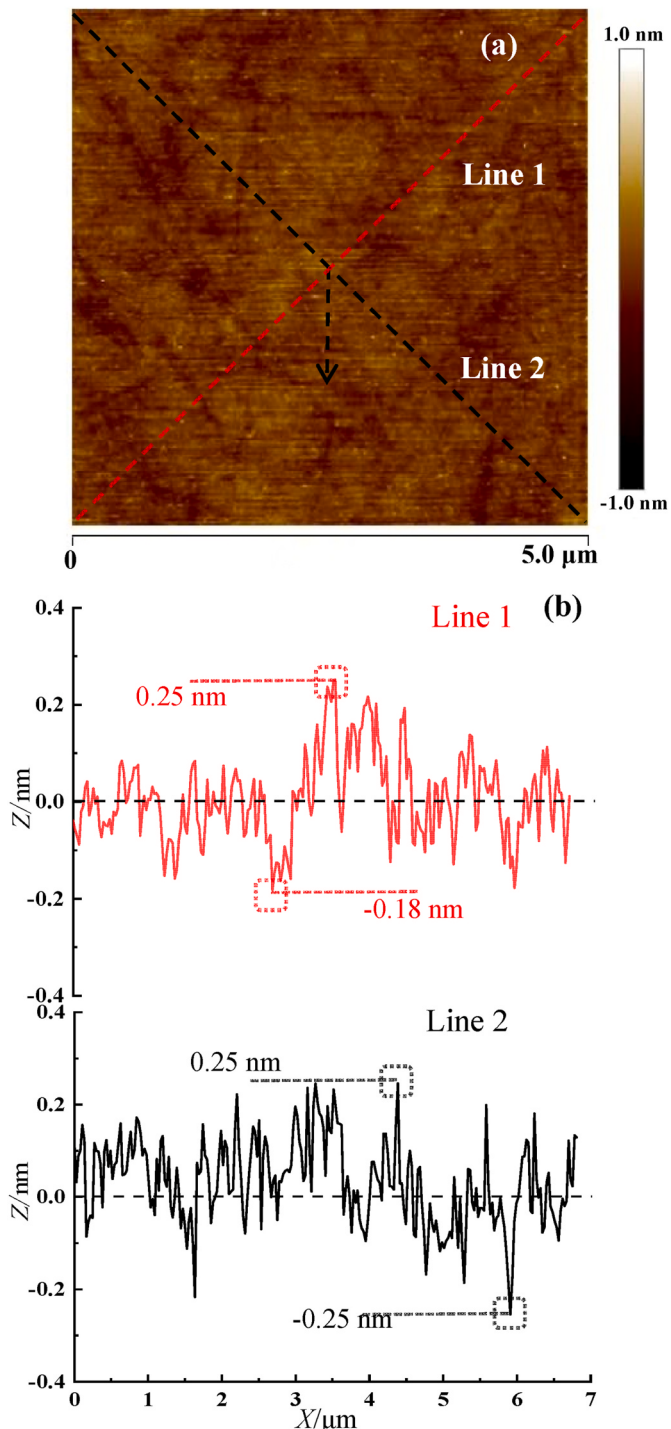


Fig. 7. 2D-AFM height image and the corresponding line-scan profiles of surfaces after CMP with pCeO₂ abrasives.

surface (Fig. 10a), most nano-sized asperity peaks were effectively removed by pCeO₂ and pCeZrO₂ abrasives (Fig. 10b–d), thereby leading to highly planarized surfaces without introducing other mechanical damages or defects. For tracking surface morphologies in a relatively large scale, the workpieces finished with pCeO₂ and pCeZrO₂ abrasives were also detected using a 3D noncontact interferometric microscope. The polished workpieces within $180.8 \times 241.0 \mu\text{m}^2$ reveal flat and smooth appearances, and the surface defects (scratches, pits, residues, etc.) can hardly be found, as shown in Fig. 11.

Removal efficiency is another critical index for CMP performance,

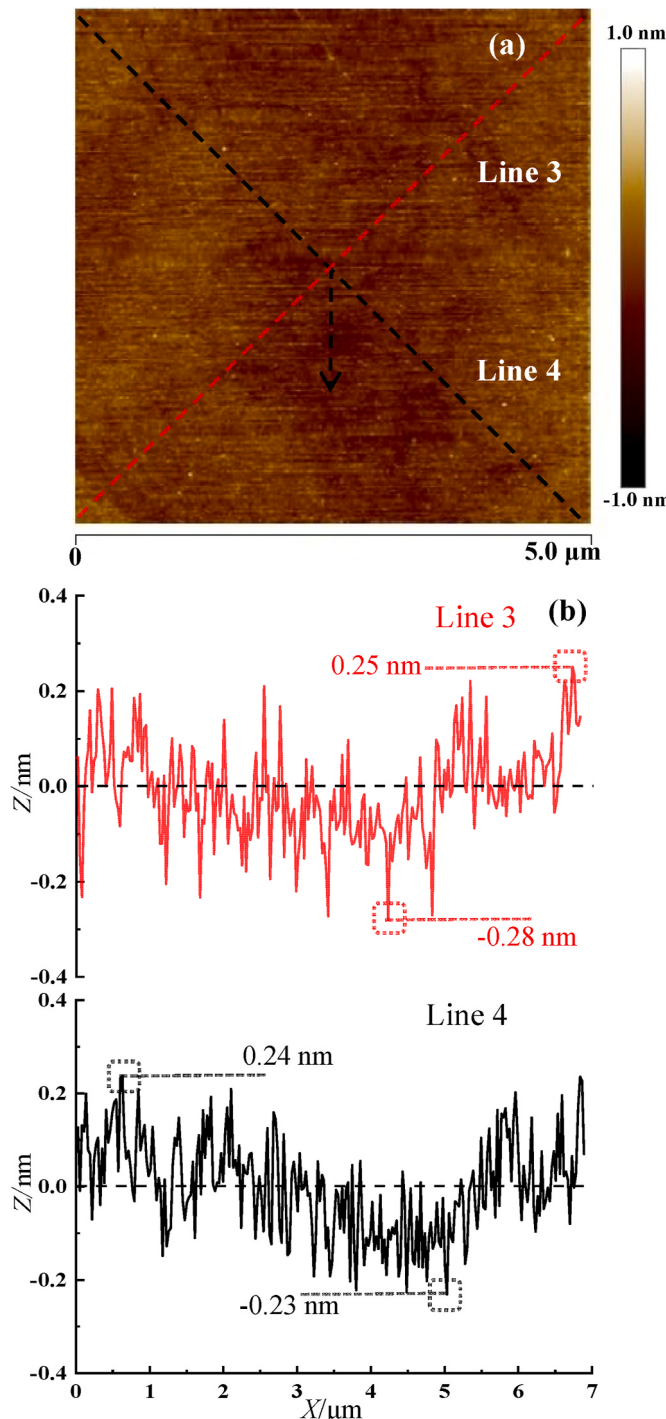


Fig. 8. 2D-AFM height image and the corresponding line-scan profiles of surfaces after CMP with pCeZrO₂ abrasives.

and the average MRR data for pure pCeO₂, pCeZrO₂, and pCeGdO₂ abrasives are shown in Fig. 12. In this work, the pCeZrO₂ and pCeGdO₂ abrasives achieve an average MRR of 88 nm/min and 109 nm/min respectively, thus leading to a 44.3% and 78.7% enhancement of MRR by comparison with the undoped pCeO₂ ones (61 nm/min). In this work, the obtained Zr- and Gd-doped pCeO₂ abrasives contribute to the oxide removal efficiency enhancement with respect to the pure pCeO₂ ones.

3.2.2. CMP mechanism of pCeO₂ abrasives

Fig. 13 presents the proposed schematic diagrams depicting the interfacial contact behavior between pCeO₂ abrasives and substrate

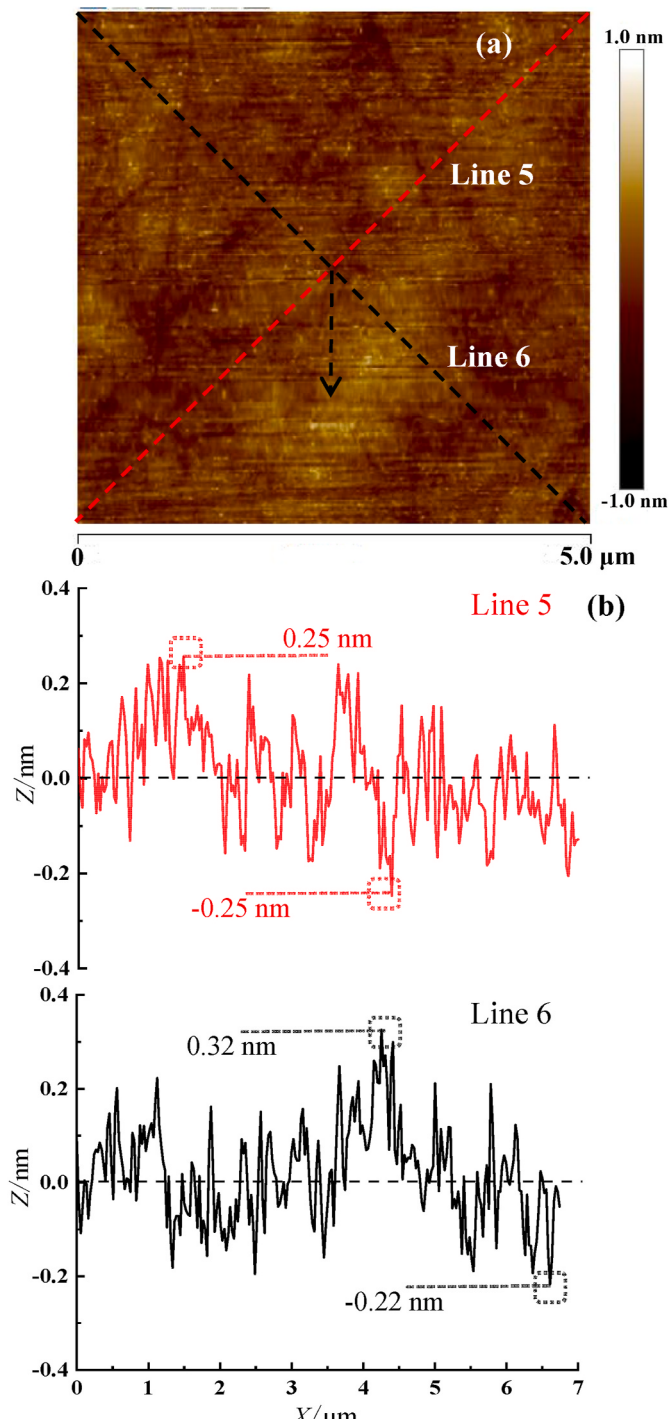


Fig. 9. 2D-AFM height image and the corresponding line-scan profiles of surfaces after CMP with pCeGdO₂ abrasives.

surfaces, the atomic surface structures and defects of the Zr- and Gd-doped pCeO₂, and the material removal mechanism for oxide-CMP with pCeO₂ abrasives.

Several investigations [35–39] focused on the effects of mechanical property (especially modulus and hardness) of abrasive particles on the achieved surface quality and MRR. Mathematical modelling and theoretical analysis results proposed that the flexible abrasives with relatively low moduli might deform elastically during the interfacial contact, friction and wear processes. It contributed to an enlarged contact area combined with a reduced contact stress and indentation depth at the tribological interface of abrasive/workpiece. Therefore, the

Table 1Surface characteristics (R_a and RMS roughness) achieved by pCeO₂, pCeZrO₂, and pCeGdO₂ abrasives.

Abrasives	R_a (nm)				RMS (nm)			
	Run 1	Run 2	Run 3	Average R_a	Run 1	Run 2	Run 3	Average RMS
pCeO ₂	0.125	0.112	0.086	0.11 ± 0.02	0.159	0.145	0.109	0.14 ± 0.03
pCeZrO ₂	0.115	0.092	0.094	0.11 ± 0.01	0.143	0.116	0.119	0.13 ± 0.01
pCeGdO ₂	0.157	0.151	0.109	0.14 ± 0.03	0.197	0.188	0.139	0.17 ± 0.03

mechanical damages or defects may be eliminated and the surface quality can be improved. MD simulation results [16] also confirmed that the porous clusters contributed to avoiding hard impact and reducing plough behavior between the particle and the surface, resulting in the plough behavior and mechanical damage reductions. By comparison with solid materials, the porous ones commonly present the evidently reduced moduli and/or hardness, which are highly tunable by adjusting their internal constructions such as pore structure, pore size, pore volume and etc. In this work, we can safely speculate that the as-obtained pCeO₂ particles also possess much low moduli with respect to the solid ones. As shown in Fig. 13a, the non-rigid pCeO₂ abrasive particles might deform elastically under an applied down pressure during CMP, thus leading to the reductions of the contact pressure at the particle-wafer interface and the indentation depth of the abrasive onto the surface. Based on the discussions described above, both pCeO₂, pCeZrO₂, and pCeGdO₂ abrasives achieve non-damage and ultra-smooth surfaces with atomic-scale roughness, possibly resulting from the optimized interface contact behavior originated from their porous structures and non-rigid properties.

Manipulating the oxygen vacancy and/or Ce³⁺ concentration is a popular strategy to optimize the physicochemical performance of CeO₂-based systems [31,40,41]. It is also confirmed that cationic variations in valence (or radius) and/or lattice distortions contribute to the oxygen vacancy and Ce³⁺ enrichments in the doped CeO₂ systems. Moreover, it is commonly believed that a mixed valence states of Ce⁴⁺ and Ce³⁺ coexist in CeO₂-based materials. In-depth investigations [42,43] further revealed that the active Ce³⁺ species (or thin Ce³⁺ layer of several nm in depth) existed at the surfaces of CeO₂ NPs. As shown in Fig. 13b, Zr- and Gd-doping treatments also contribute to the oxygen vacancy and Ce³⁺ enrichments at CeO₂ surfaces, resulting from the reductions of the total positive charges and the oxygen vacancy formation energy of CeO₂.

The material removal mechanism of CeO₂ toward SiO₂ can be interpreted by means of the dynamic formation and circular breakage of Ce–O–Si bonds, resulting from the water-associated tribochemical reaction between CeO₂–SiO₂ interface [44] and the well-known chemical-tooth effect proposed by Cook [45]. In oxide removal processes [45–48], the hydrolysis of SiO₂ might occur at weakly alkaline conditions (Reaction 1).



The oxygen vacancies at CeO₂ surfaces could react with water to form surface hydroxyl groups, which further reacted with the Si–O[−] sites at SiO₂ films to create temporary Ce–O–Si bonds (Reaction 2).



Consequently, the effective oxide removal can be achieved via the dynamic formation and breakage of Ce–O–Si bonding (so-called solid-state tribochemical reaction), as shown in Fig. 13c.

The structural defects in CeO₂, such as Ce³⁺ and oxygen vacancy, play a key role in determining the potential applications and attractive characteristics of CeO₂-based materials. And the surface defects (typically Ce³⁺ and oxygen vacancy) of CeO₂ NPs can also be created and controlled by metal-doping treatments [31,41,42,49,50]. In oxide-CMP applications, the experimental investigations and theoretical simulations [18,19,21,22,44–48,51–55] confirmed that the formed Ce³⁺ and oxygen vacancy at CeO₂ abrasive surfaces contributed to the

enhancement of tribochemical activity between CeO₂–SiO₂, thereby leading to an improved of material removal efficiency. Recently, Kim and coworkers [21,22] proposed the improved removal rate in oxide-CMP by forming oxygen vacancies in CeO₂ abrasives via UV-irradiation or lanthanide (La and Nd)-doping treatment. As revealed by X-ray photoelectron spectroscopy and UV-visible absorption spectroscopy, more oxygen vacancies led to increased Ce³⁺ contents at the surfaces of CeO₂ nanoparticles after UV-irradiation treatments. Furthermore, it was also confirmed that the removal rate of CeO₂ against SiO₂ gradually raised as the Ce³⁺ and/or oxygen vacancy concentrations increased. There was a reliable correlation between the removal efficiency and the CeO₂ surface defects (typically Ce³⁺ and oxygen vacancy).

In this work, both Raman and UV-vis-DRS spectra indicate that Zr- and Gd-doping in pCeO₂ are responsible for the formation of more oxygen vacancies, thereby leading to more Ce³⁺ as reactive sites. And the pCeGdO₂ NPs possess the highest Ce³⁺ and oxygen vacancy concentrations. The increased surface defects (reactive sites) are expected to improve the tribochemical activity of pCeO₂ abrasives and promote the chemical bonding between ceria and silica, thus accelerating the formation and breakage of Ce–O–Si bonds. Consequently, the as-prepared pCeZrO₂ and pCeGdO₂ abrasives achieved the improvement of material removal toward silica films by comparison with the undoped pCeO₂ ones. As confirmed by N₂ adsorption-desorption measurements, the pCeZrO₂ (6.9 nm) and pCeGdO₂ NPs (8.1 nm) also present a larger average pore-size than that of the undoped pCeO₂ (5.1 nm). According to the MD simulations [16], the enlarged pore-size might also contribute to the increased actual contact areas between porous abrasives and substrate surfaces, possibly resulting from the elastic deform of low-modulus particles. In addition, the expanded pore-size might also contribute to the enhanced adhesion and pulling effects of abrasives to surfaces. Furthermore, the water-involved tribochemical wear [56] might occur at interfacial contact, and thus facilitate the tribochemical reaction and material removal. All these factors are beneficial to the MRR increasement for the Zr- and Gd-doped pCeO₂ abrasives. By comparison with pure pCeO₂ (61 nm/min) and pCeZrO₂ (88 nm/min), the highest MRR (109 nm/min) achieved by pCeGdO₂ abrasives may be attributed to the enhanced oxygen vacancy and Ce³⁺ concentrations, as well as the expanded pore diameter.

This work provides promising and effective CeO₂-based abrasive materials having good potential of practical applications for achieving high-quality and high-efficiency oxide-CMP. Further works on the structure, component, property optimizations, as well as the oxide removal mechanism of pure and doped pCeO₂ abrasives are ongoing in our group.

4. Conclusions

1. Nanosized porous CeO₂ (pCeO₂), pCeZrO₂, and pCeGdO₂ spherical abrasives were prepared via a hydrothermal approach and applied in oxide-CMP applications. The pure pCeO₂ abrasives achieved the ultra-smooth and non-damage surfaces with average roughness of 0.11 nm R_a and 0.14 nm RMS, which were comparable to those of pCeZrO₂ (0.11 nm R_a , 0.13 nm RMS) and pCeZrO₂ (0.14 nm R_a , 0.17 nm RMS).
2. The developed abrasives contributed to the topographical variation reductions, the surface planarization improvements, as well as the

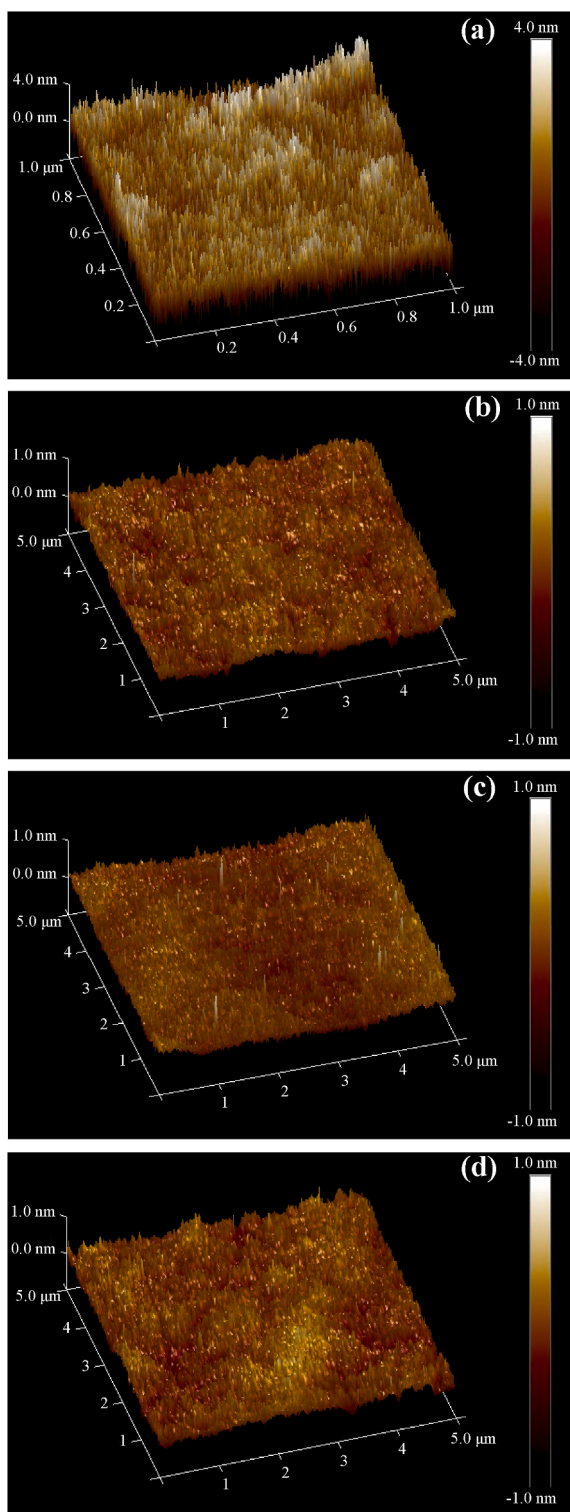


Fig. 10. 3D-AFM images of the surfaces (a) before and after CMP with (b) pCeO₂, (c) pCeZrO₂, (d) pCeGdO₂ abrasives.

surface defect eliminations. It might be attributed to the enlarged contact area, reduced contact stress, and decreased indentation depth between abrasives and surfaces, possibly originating from their porous nanostructures and non-rigid characteristics.

3. As expected, the pCeZrO₂ (88 nm/min) and pCeGdO₂ abrasives (109 nm/min) achieved ca. 44.3% and 78.7% MRR increments compared to the undoped pCeO₂ (61 nm/min). After Zr- and Gd-doping, the

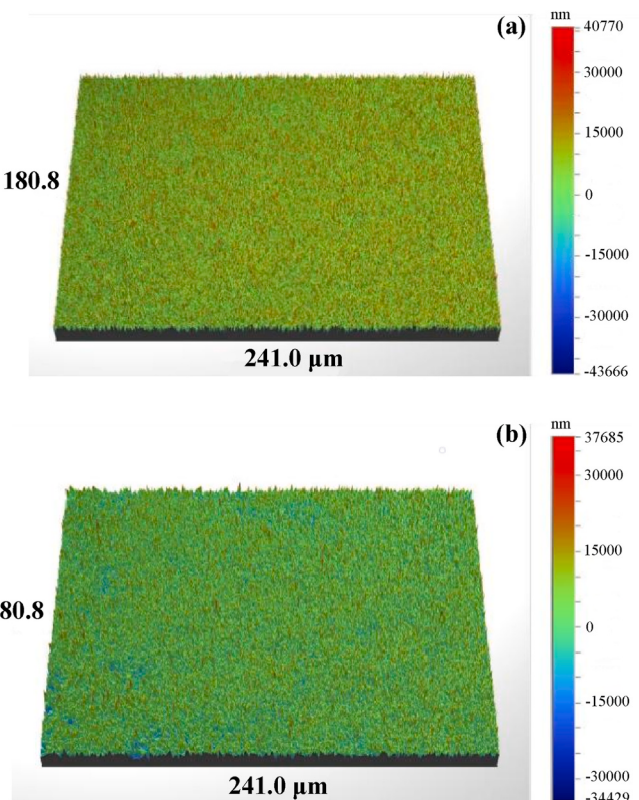


Fig. 11. Morphologies within 180.8 × 241.0 μm^2 of the surfaces after CMP with (a) pCeO₂ and (b) pCeZrO₂ abrasives.

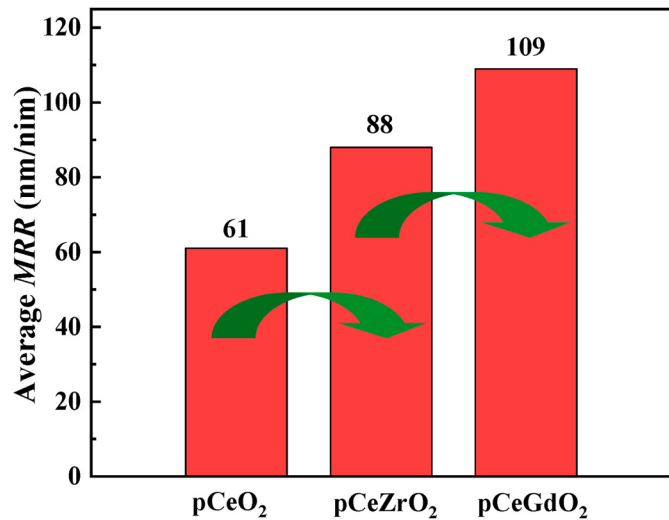


Fig. 12. Average MRR data achieved by pCeO₂, pCeZrO₂, and pCeGdO₂ abrasives.

Ce³⁺ and oxygen vacancy enrichments might be responsible for the enhanced oxide removal efficiency of pCeO₂ abrasives, possibly resulting from the improved tribochemical activity between CeO₂-SiO₂.

4. More direct and solid evidence is still needed to explore the relation among the structure characteristics (specific area, pore size, porosity, etc.), mechanical properties (hardness, modulus, etc.), surface chemistry (typically Ce³⁺ and oxygen vacancy) and oxide-CMP performance of pCeO₂ abrasives.

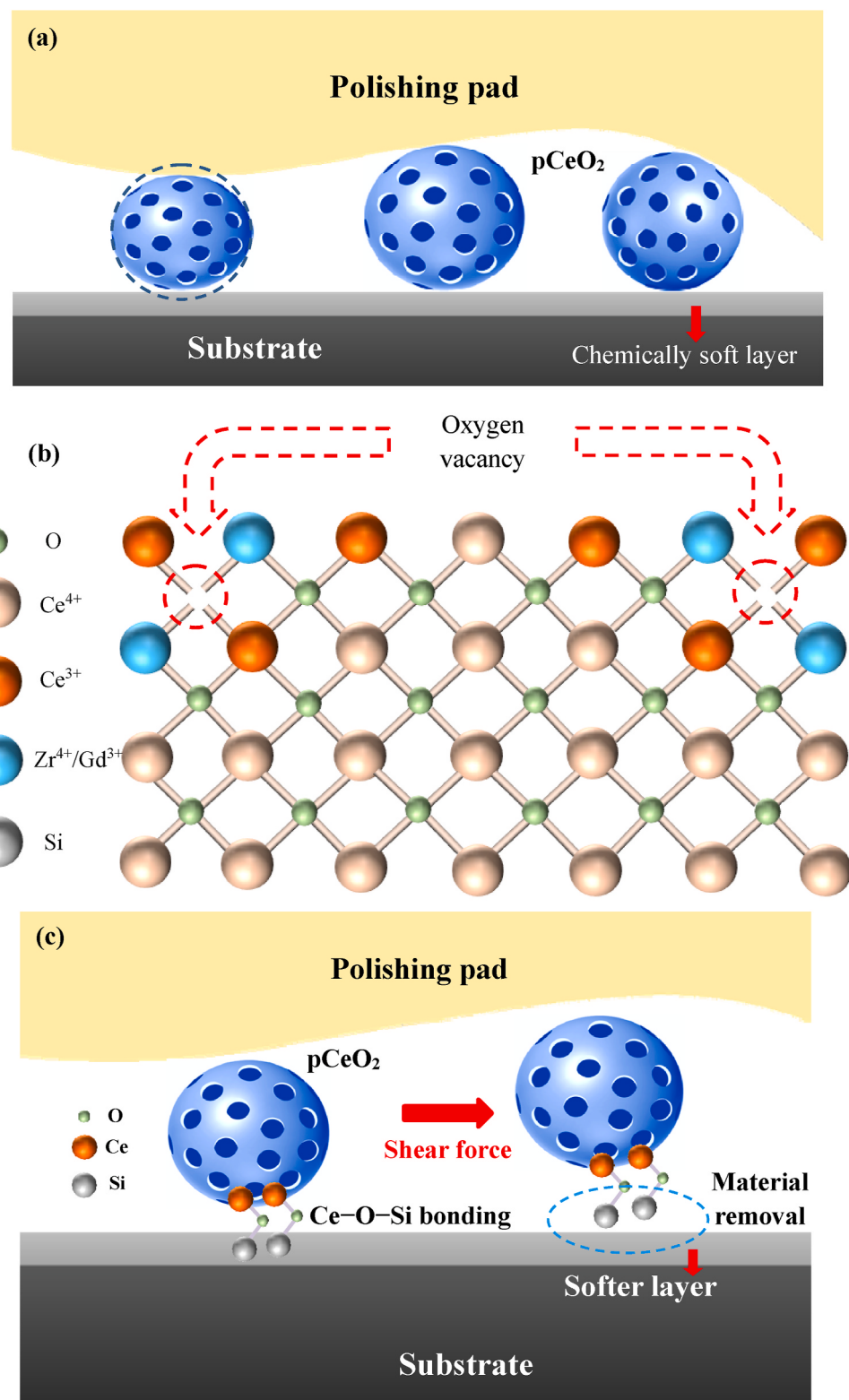


Fig. 13. Schematics of (a) the interfacial contact behavior between pCeO₂ abrasives and substrate surfaces, (b) the atomic surface structures and defects of the Zr- or Gd-doped pCeO₂, and (c) the material removal mechanism for oxide-CMP with pCeO₂ abrasives.

Declaration of competing interest

The authors declare that they have no known competing financial interests or personal relationships that could have appeared to influence the work reported in this paper.

Acknowledgements

The paper is supported financially by National Natural Science Foundation of China (Grant Nos. 51575058 and 51875052), and the Priority Academic Program Development of Jiangsu Higher Education Institutions (PAPD).

References

- [1] M. Krishnan, J.W. Nalaskowski, L.M. Cook, Chemical mechanical planarization: slurry chemistry, materials, and mechanisms, *Chem. Rev.* 110 (2010) 178–204.
- [2] L. Liao, Z. Zhang, F. Meng, D. Liu, B. Wu, Y. Li, W. Xie, A novel slurry for chemical mechanical polishing of single crystal diamond, *Appl. Surf. Sci.* 564 (2021) 150431.
- [3] H. Aida, H. Takeda, T. Doi, Analysis of mechanically induced subsurface damage and its removal by chemical mechanical polishing for gallium nitride substrate, *Precis. Eng.* 67 (2021) 350–358.
- [4] Q. Mu, Z. Jin, X. Han, Y. Yan, Z. Zhang, P. Zhou, Effects of slurry pH on chemical and mechanical actions during chemical mechanical polishing of YAG, *Appl. Surf. Sci.* 563 (2021) 150359.
- [5] C. Deng, L. Jiang, N. Qin, L. Qian, Effects of pH and H_2O_2 on the chemical mechanical polishing of titanium alloys, *J. Mater. Process. Technol.* 295 (2021) 117204.
- [6] H. Lei, X. Wu, R. Chen, Preparation of porous alumina abrasives and their chemical mechanical polishing behavior, *Thin Solid Films* 520 (2012) 2868–2872.
- [7] H. Lei, L. Jiang, R. Chen, Preparation of copper-incorporated mesoporous alumina abrasive and its CMP behavior on hard disk substrate, *Powder Technol.* 219 (2012) 99–104.
- [8] L. Huang, Z. Wang, H. Lei, R. Chen, Preparation of porous alumina-g-polystyrene sulfonic acid abrasive and its chemical mechanical polishing behavior on hard disk substrate, *Microelectron. Eng.* 116 (2014) 11–16.
- [9] H. Li, H. Lei, R. Chen, Preparation of porous Fe_2O_3/SiO_2 nanocomposite abrasives and their chemical mechanical polishing behaviors on hard disk substrates, *Thin Solid Films* 520 (2012) 6174–6178.
- [10] B. Zhao, W. Ding, Z. Chen, C. Yang, Pore structure design and grinding performance of porous metal-bonded CBN abrasive wheels fabricated by vacuum sintering, *J. Manuf. Process.* 44 (2019) 125–132.
- [11] M.Y. Tsai, Z.T. Hoo, Polishing single-crystal silicon carbide with porous structure diamond and graphene-TiO₂ slurries, *Int. J. Adv. Manuf. Technol.* 105 (2019) 1519–1530.
- [12] Y. Chen, Z. Li, J. Qin, A. Chen, Monodispersed mesoporous silica ($mSiO_2$) spheres as abrasives for improved chemical mechanical planarization performance, *J. Mater. Sci.* 51 (2016) 5811–5822.
- [13] J. Ryu, W. Kim, J. Yun, K. Lee, J. Lee, H. Yu, J.H. Kim, J.J. Kim, J. Jang, Fabrication of uniform wrinkled silica nanoparticles and their application to abrasives in chemical mechanical planarization, *ACS Appl. Mater. Interfaces* 10 (2018) 11843–11851.
- [14] Y. Chen, X. Ma, W. Cai, A. Chen, Preparation of three-dimensional dendritic-like mesoporous silica particles and their pore size-dependent polishing behavior and mechanism, *J. Porous Mater.* 26 (2019) 1869–1877.
- [15] P. Gao, T. Liu, Z. Zhang, F. Meng, R.P. Ye, J. Liu, Non-spherical abrasives with ordered mesoporous structures for chemical mechanical polishing, *Sci. China Mater.* 64 (2021) 2747–2763.
- [16] R. Chen, R. Jiang, H. Lei, M. Liang, Material removal mechanism during porous silica cluster impact on crystal silicon substrate studied by molecular dynamics simulation, *Appl. Surf. Sci.* 264 (2013) 148–156.
- [17] X. Feng, D.C. Sayle, Z.L. Wang, M.S. Paras, B. Santora, A.C. Sutorik, T.X.T. Sayle, Y. Yang, Y. Ding, X. Wang, Y. Her, Converting ceria polyhedral nanoparticles into single-crystal nanospheres, *Science* 312 (2006) 1504–1508.
- [18] S.R. Alety, K.V. Sagi, S.V. Babu, Role of Ce³⁺ ions in achieving high silicon nitride polish rates, *ECS J. Solid State Sci. Technol.* 6 (2017) P898–P903.
- [19] J. Cheng, S. Huang, Y. Li, T. Wang, L. Xie, X. Lu, RE (La, Nd and Yb) doped CeO₂ abrasive particles for chemical mechanical polishing of dielectric materials: experimental and computational analysis, *Appl. Surf. Sci.* 506 (2020) 144668.
- [20] Y. Chen, Z. Mu, W. Wang, A. Chen, Development of mesoporous SiO₂/CeO₂ core-shell nanoparticles with tunable structures for non-damage and efficient polishing, *Ceram. Int.* 46 (2020) 4670–4678.
- [21] E. Kim, J. Hong, S. Hong, C. Kanade, H. Seok, H. Kim, T. Kim, Improvement of oxide removal rate in chemical mechanical polishing by forming oxygen vacancy in ceria abrasives via ultraviolet irradiation, *Mater. Chem. Phys.* 273 (2021) 124967.
- [22] E. Kim, J. Lee, C. Bae, H. Seok, H. Kim, T. Kim, Effects of trivalent lanthanide (La and Nd) doped ceria abrasives on chemical mechanical polishing, *Powder Technol.* (2021), <https://doi.org/10.1016/j.powtec.2021.11.069>.
- [23] X. Liang, J. Xiao, B. Chen, Y. Li, Catalytically stable and active CeO₂ mesoporous spheres, *Inorg. Chem.* 49 (2010) 8188–8190.
- [24] Y. Chen, R. Long, Polishing behavior of PS/CeO₂ hybrid microspheres with controlled shell thickness on silicon dioxide CMP, *Appl. Surf. Sci.* 257 (2011) 8679–8685.
- [25] Y. Chen, J. Qin, Y. Wang, Z. Li, Core/shell composites with polystyrene cores and meso-silica shells as abrasives for improved chemical mechanical polishing behavior, *J. Nanoparticle Res.* 17 (2015) 363.
- [26] Y. Xu, N. Farandos, M. Rosa, P. Zielke, V. Esposito, P. Vang Hendriksen, S. H. Jensen, T. Li, G. Kelsall, R. Kiebach, Continuous hydrothermal flow synthesis of Gd-doped CeO₂ (GDC) nanoparticles for inkjet printing of SOFC electrolytes, *Int. J. Appl. Ceram. Technol.* 15 (2018) 315–327.
- [27] S. Shi, S. Zhou, S. Liu, Z. Chen, Photocatalytic activity of erbium-doped CeO₂ enhanced by reduced graphene oxide/CuO cocatalyst for the reduction of CO₂ to methanol, *Environ. Prog. Sustain.* 37 (2018) 655–662.
- [28] B. Liu, C. Li, G. Zhang, X. Yao, S.S.C. Chuang, Z. Li, Oxygen vacancy promoting dimethyl carbonate synthesis from CO₂ and methanol over Zr-doped CeO₂ nanorods, *ACS Catal.* 8 (2018) 10446–10456.
- [29] C. Artini, M.M. Carnasciali, J.R. Plaisier, G.A. Costa, M. Pani, A novel method for the evaluation of the rare earth (RE) coordination number in RE-doped ceria through Raman spectroscopy, *Solid State Ionics* 311 (2017) 90–97.
- [30] R.C. Maher, G. Kerherve, D.J. Payne, X. Yue, P.A. Connor, J. Irvine, L.F. Cohen, The reduction properties of M-doped (M=Zr, Gd) CeO₂/YSZ scaffolds co-infiltrated with nickel, *Energy Technol-GER.* 6 (2018) 2045–2052.
- [31] R. Tao, J. Xu, H. Zhong, W. Wen, Q. Pan, Y. Liu, J. Chen, Finely tuned structure and catalytic performance of cerium oxides by a continuous samarium doping from 0 to 100, *Inorg. Chem.* 58 (2019) 13066–13076.
- [32] C. Mao, Y. Zhao, X. Qiu, J. Zhu, C. Burda, Synthesis, characterization and computational study of nitrogen-doped CeO₂ nanoparticles with visible-light activity, *Phys. Chem. Chem. Phys.* 10 (2008) 5633–5638.
- [33] P. Patsalas, S. Logothetidis, L. Sygellou, S. Kennou, Structure-dependent electronic properties of nanocrystalline cerium oxide films, *Phys. Rev. B* 68 (2003), 035104.
- [34] H. Wei, E.F. Rodriguez, A.F. Hollenkamp, A.I. Bhatt, D. Chen, R.A. Caruso, High reversible pseudocapacity in mesoporous yolk-shell anatase TiO₂/TiO₂(B) microspheres used as anodes for Li-ion batteries, *Adv. Funct. Mater.* 27 (2017) 1703270.
- [35] X. Chen, Y. Zhao, Y. Wang, Modeling the effects of particle deformation in chemical mechanical polishing, *Appl. Surf. Sci.* 258 (2012) 8469–8474.
- [36] Y. Chen, Z. Li, N. Miao, Synergetic effect of organic cores and inorganic shells for core/shell structured composite abrasives for chemical mechanical planarization, *Appl. Surf. Sci.* 314 (2014) 180–187.
- [37] C. Qin, Z. Hu, A. Tang, Z. Yang, S. Luo, An efficient material removal rate prediction model for cemented carbide inserts chemical mechanical polishing, *Wear* 452–453 (2020) 203293.
- [38] B. Gao, W. Zhai, Q. Zhai, Y. Shi, Polystyrene/CeO₂ core/shell abrasives for high-quality 4H-SiC surface in ECMP: the effects of shell thickness, *ECS J. Solid State Sci. Technol.* 9 (2020), 044005.
- [39] H. Chen, L. Zhang, M. Li, G. Xie, Synthesis of core-shell micro/nanoparticles and their tribological application: a review, *Materials* 13 (2020) 4590.
- [40] J. Paier, C. Penschke, J. Sauer, Oxygen defects and surface chemistry of ceria: quantum chemical studies compared to experiment, *Chem. Rev.* 113 (2013) 3949–3985.
- [41] Y. Shi, L. Wang, Z. Wang, G. Vinai, L. Braglia, P. Torelli, C. Aruta, E. Traversa, W. Liu, N. Yang, Defect engineering for tuning the photoresponse of ceria-based solid oxide photoelectrochemical cells, *ACS Appl. Mater. Interfaces* 13 (2021) 541–551.
- [42] Y. Lin, Z. Wu, J. Wen, K.R. Poeppelmeier, L.D. Marks, Imaging the atomic surface structures of CeO₂ nanoparticles, *Nano Lett.* 14 (2014) 191–196.
- [43] B. Goris, S. Turner, S. Bals, G. Van Tendeloo, Three-dimensional valency mapping in ceria nanocrystals, *ACS Nano* 8 (2014) 10878–10884.
- [44] T. Onodera, H. Takahashi, S. Nomura, First-principles molecular dynamics investigation of ceria/silica sliding interface toward functional materials design for chemical mechanical polishing process, *Appl. Surf. Sci.* 530 (2020) 147259.
- [45] L.M. Cook, Chemical processes in glass polishing, *J. Non-Cryst. Solid* 120 (1990) 152–171.
- [46] T. Hoshino, Y. Kurata, Y. Terasaki, K. Susa, Mechanism of polishing of SiO₂ films by CeO₂ particles, *J. Non-Cryst. Solids* 283 (2001) 129–136.
- [47] C.M. Netzband, K. Dunn, Controlling the cerium oxidation state during silicon oxide CMP to improve material removal rate and roughness, *ECS J. Solid State Sci. Technol.* 9 (2020), 044001.
- [48] C.M. Netzband, K. Dunn, Investigation into the effect of CMP slurry chemicals on ceria abrasive oxidation state using XPS, *ECS J. Solid State Sci. Technol.* 8 (2019) P629–P633.
- [49] J. Koettgen, S. Grieshammer, G. Dück, G. Ulbrich, M. Lerch, M. Martin, Ab initio and experimental oxygen ion conductivities in Sm-Zr and Gd-Zr co-doped ceria, *Solid State Ionics* 355 (2020) 115422.
- [50] Y. Liu, R. Zhang, Study of doped mesoporous ceria with tailored oxygen vacancies for enhances activity for ethylbenzene oxidation application, *Colloids Surf., A* 603 (2020) 125163.
- [51] O. Nobuki, I. Muneyuki, N. Miho, M. Kubo, Polishing process simulation of SiO₂ by CeO₂ abrasive grain under wet environment, *Hyomen Kagaku* 33 (2012) 351–356.
- [52] P. Janos, J. Ederer, V. Pilarova, J. Henych, J. Tolasz, D. Milde, T. Opletal, Chemical mechanical glass polishing with cerium oxide: effect of selected physico-chemical characteristics on polishing efficiency, *Wear* 362 (2016) 114–120.
- [53] Y. Chen, W. Cai, W. Wang, A. Chen, Preparation, characterization, and application of dendritic silica-supported samarium-doped ceria nanoparticles in ultra-precision polishing for silica films, *J. Nanoparticle Res.* 21 (2019) 226.
- [54] Y. Chen, C. Zuo, Z. Li, A. Chen, Design of ceria grafted mesoporous silica composite particles for high-efficiency and damage-free oxide chemical mechanical polishing, *J. Alloys Compd.* 736 (2018) 276–288.
- [55] A. Chen, Y. Duan, Z. Mu, W. Cai, Y. Chen, Meso-silica/Erbium-doped ceria binary particles as functionalized abrasives for photochemical mechanical polishing (PCMP), *Appl. Surf. Sci.* 550 (2021) 149353.
- [56] L. Chen, L. Qian, Role of interfacial water in adhesion, friction, and wear-A critical review, *Friction* 9 (2020) 1–28.